

Smol-GS: Compact Representations for Abstract 3D Gaussian Splatting

Haishan Wang, Mohammad Hassan Vali, and Arno Solin
 ELLIS Institute Finland and Aalto University, Espoo, Finland
 {haishan.wang, mohammad.vali, arno.solin}@aalto.fi

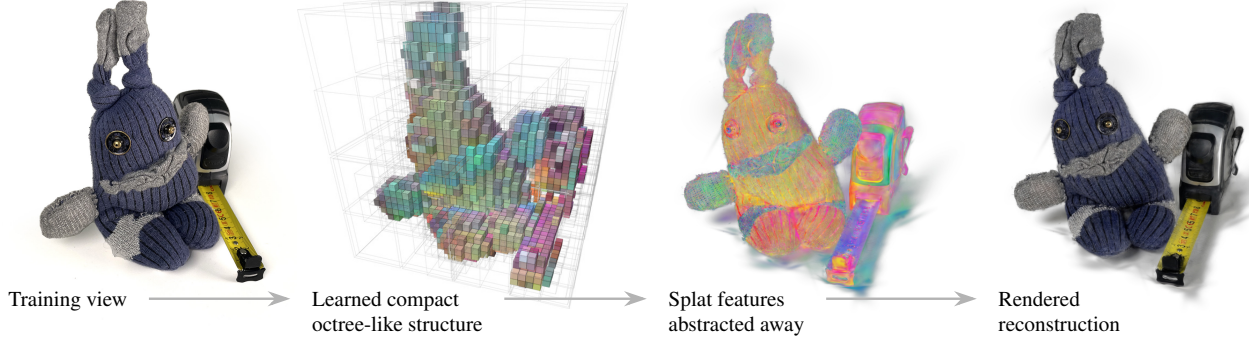


Figure 1. **Smol-GS** learns a compact representation of the 3D scene that (i) stores coordinates in an efficient octree-like structure and (ii) abstracts away view-dependent splat features such as color, shape, and material cues. We visualize the abstract 8-dimensional features f in the second and third panel by coloring $\text{RGB} = \text{sigmoid}(\text{PCA}(\mathbf{f}))$, which reveals structure in the encodings. On the MIP-NeRF 360 benchmark, the current state-of-the-art compresses from 734 MB (vanilla 3DGS) to 8.74 MB (HAC++), while Smol-GS only needs 4.75 MB.

Abstract

We present *Smol-GS*, a novel method for learning compact representations for 3D Gaussian Splatting (3DGS). Our approach learns highly efficient encodings in 3D space that integrate both spatial and semantic information. The model captures the coordinates of the splats through a recursive voxel hierarchy, while splat-wise features store abstracted cues, including color, opacity, transformation, and material properties. This design allows the model to compress 3D scenes by orders of magnitude without loss of flexibility. Smol-GS achieves state-of-the-art compression on standard benchmarks while maintaining high rendering quality. Beyond visual fidelity, the discrete representations could potentially serve as a foundation for downstream tasks such as navigation, planning, and broader 3D scene understanding.

Project page: <https://aaltoml.github.io/Smol-GS>

1. Introduction

3D Gaussian Splatting (3DGS, [18]) is a paradigm for novel view synthesis that models a scene as a set of rasterized Gaussian splats. It achieves real-time speed and high rendering quality through rasterization techniques [22]. However,

3DGS suffers from memory inefficiency; it often requires several gigabytes of storage with millions of splats to represent complex scenes. This issue related to the large memory footprint has been tackled extensively in recent work [4, 5, 7, 8, 11, 23, 25, 28, 29, 32–34, 36, 38, 45, 46, 51, 55]. These methods improve compactness to varying degrees, yet the coordinate data and high-dimensional appearance cues remain hard to store efficiently at scale.

Two directions dominate current 3DGS compression: (i) Signal-processing approaches quantize or vector-quantize splat attributes and deliver sizable savings [7, 23, 32–34, 45]. (ii) Learning-based approaches compress by sharing structure across splats, with anchor-offset hierarchies from Scaffold-GS [27] forming the backbone of the most competitive results [4, 5, 25, 46]. However, signal-processing pipelines do not fully exploit local spatial correlations and repeated patterns among splats, and anchor-offset designs can introduce transparent or invisible offsets and extra heuristics, while often sidestepping coordinate compression because reconstruction is sensitive to coordinate errors. We revisit this premise (see Fig. 1). Our work hinges on the realization that keeping the spatial structure explicit (but efficiently packed) and abstracting the splat-wise visual features away can result in highly efficient compression.

In this paper, inspired by neural Gaussian generation in

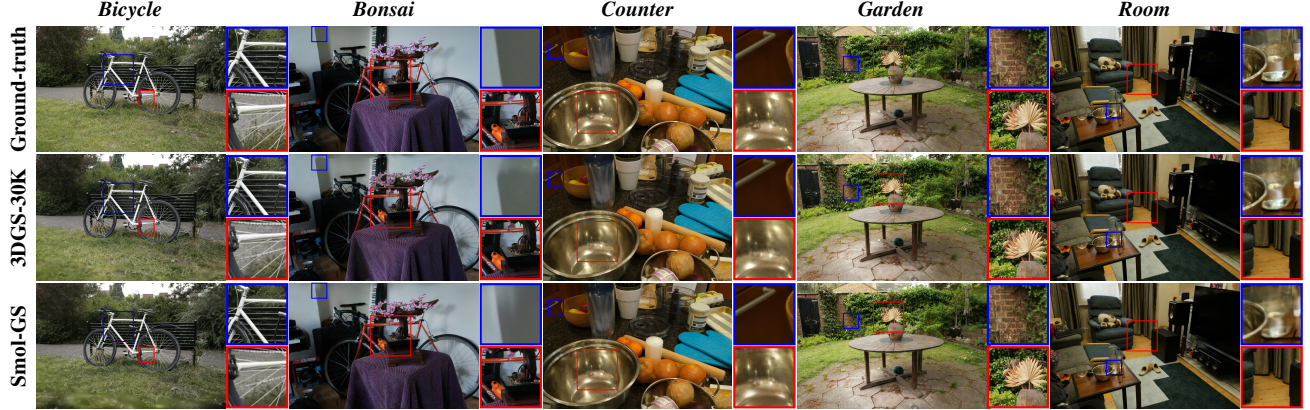


Figure 2. **Qualitative results on the MIP-NERF 360 data set.** Smol-GS provides high-fidelity reconstructions even outperforming vanilla 3DGS-30K in representing details in reflective, transparent, and low-texture regions. Smol-GS preserves sharp edges and material effects (specular highlights, glass, flat walls) while using an orders of magnitude smaller model. We include quantitative summary results in [Table 1](#).

anchor-based systems [27] and by point-cloud geometry compression [39], we propose Smol-GS. The method learns a compact representation with splat-wise abstract features and a few tiny MLPs, while compressing coordinates and features. Coordinates are stored with an occupancy-octree and entropy coding; features (color, opacity, transformation, and material cues) are quantized and entropy-coded with distributions predicted from hashed spatial descriptors. The design removes anchor-offset overhead, reduces redundancy further, and enables splat-level operations such as 3D editing and generation. Smol-GS compresses the scene while qualitative (see [Fig. 2](#)) and quantitative comparisons ([Fig. 7](#) and [Table 1](#)) show that Smol-GS matches rendering quality while pushing model size down to the smallest among strong baselines.

Contributions Our contributions can be summarized as:

- We introduce Smol-GS, a novel 3DGS compression method. It provides a simple yet effective strategy for representing 3D scenes with highly compact, splat-wise abstract features and tiny MLPs.
- We show that Smol-GS substantially reduces the storage requirements for 3DGS while maintaining high rendering quality, through both quantitative and qualitative comparisons with the state-of-the-art.
- We provide a flexible hierarchy: the octree recursion provides a means to trade fidelity for size when needed, which is valuable for low-resource devices and applications with tight memory budgets.

2. Related Work

3D Gaussian Splatting The 3DGS paradigm represents a scene as a collection of Gaussian splats initialized via structure-from-motion (SfM, [40]), based on computer graphics research [47, 58]. Each splat is associated with a location, covariance (via scale and rotation), opacity, color,

and view-dependent material properties (spherical harmonics, SH). The explicit primitive and Gaussian rasterization allow real-time rendering, while the continuous representation yields high image quality. These advantages make 3DGS a promising framework for broad applications, such as SLAM [13, 14, 17, 50], 3D editing [3, 41, 49, 56], and VR [16, 42, 54, 57].

Compaction vs. Attribute Compression Resolving the challenging memory footprint of storing the splat-wise parameters has mainly focused on two lines of research. *Compaction* reduces the number of splats via pruning and regularization, often guided by opacity, scale, importance estimation [8, 28, 36, 38, 55]. This can save memory but risks losing thin structures and requires heuristics. *Attribute compression* keeps the splat set but encodes attributes more efficiently, balancing rate and fidelity. For example, vector-quantization [10, 43, 44] based methods utilize clustering algorithms [24, 26] to compress per-splat attributes (*e.g.*, color/SH, opacity, scale/rotation) using codebooks [7, 23, 32–34]. However, traditional tools cannot eliminate the information redundancy hidden in continuity and correlation in 3D space.

Learned Compact Representations Anchor-offset hierarchies introduced by Scaffold-GS [27] condense local neighborhoods into shared anchor embeddings and reconstruct splat features with small MLPs. Follow-ups add stronger coding: HAC++ [5] and HEMGS [25] use entropy models, and ContextGS [46] leverages autoregressive anchors to reduce storage further. These methods are effective because they share structure across splats and model statistics. However, the anchors always introduce a certain ratio of transparent offsets, and the recovery of splat coordinates requires the composition of three factors: anchor location, relative coordinates, and scaling control. These design drawbacks, stemming from heuristic complications, limit the compression ratio and flexibility for downstream applications.

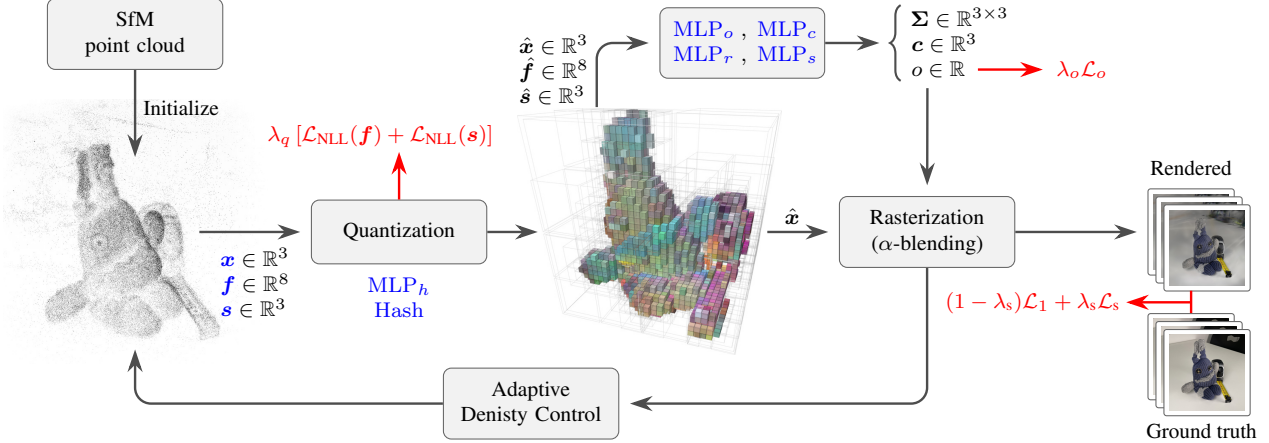


Figure 3. **Method overview of Smol-GS:** We train (trained parameters in blue) neural splats with tiny MLP-decoders for view-dependent rendering (Sec. 3.1). The coordinates are compressed with occupancy-octree coordinate coding (Sec. 3.2). We also learn the quantization and arithmetic coding of splat features with NLL rate terms (Sec. 3.3), and employ adaptive density control with stage-wise training (loss-terms in red) to balance fidelity and size (Secs. 3.4 and 3.5).

Additionally, the methods typically avoid compressing coordinates due to quality sensitivity, which limits the efficiency of compression.

Coordinate Compression and Geometry Coding Point-cloud geometry compression shows that hierarchical occupancy enables compact, often lossless storage of 3D locations via octrees [6, 9, 37, 39]. This perspective suggests that 3DGS coordinates—despite their importance for fidelity—can also be stored efficiently using an occupancy-octree with entropy coding [15], leaving appearance and view-dependent effects to learned low-dimensional features.

Smol-GS departs from anchor-offset designs by (i) encoding coordinates with an occupancy-octree plus entropy coding, and (ii) compressing splat-wise abstract features (color, opacity, transformation, and material cues) via learned quantization and entropy coding, reconstructed through tiny MLPs. Smol-GS aims to keep the data exploitation capability of learning-based methods, and real-time rendering speed and editing capabilities from explicit primitives modeling.

3. Methods

Smol-GS consists of four parts that work together (see Fig. 3 for an overview): (i) *Tiny decoders* (Sec. 3.1): Small MLPs reconstruct view-dependent color and transformation from abstract features and viewing direction, keeping rendering fast. (ii) *Coordinate encoding* (Sec. 3.2): Splat coordinates are stored with an occupancy-octree and entropy coding, leveraging spatial sparsity while avoiding anchor overhead. (iii) *Feature compression* (Sec. 3.3): Low-dimensional per-splat features capture color, opacity, transformation, and material cues. They are quantized with learned step sizes and encoded arithmetically. (iv) *Adaptive density control and training* (Secs. 3.4 and 3.5): Gradient-based densification, prun-

ing, and stage-wise optimization balance fidelity and size.

3.1. Neural Gaussian Splats

Smol-GS models the 3D scene as a set of neural Gaussian splats with the support of a few MLPs (MLP_o , MLP_c , MLP_s , MLP_r). Each splat has a coordinate $\mathbf{x} \in \mathbb{R}^3$, a feature vector $\mathbf{f} \in \mathbb{R}^{n_f}$ (we use $n_f = 8$ in practice, see Sec. 4.2), and a scaling controller $\mathbf{s} \in \mathbb{R}^3$. The feature \mathbf{f} encodes abstract, splat-wise cues including optical information, geometric transformation, and orientation-induced material properties.

Given the camera center coordinate \mathbf{x}_c during rendering, we first concatenate the feature vector with the view,

$$\mathbf{f}^* = \text{concat}(\mathbf{f}, \frac{\mathbf{x}_c - \mathbf{x}}{\|\mathbf{x}_c - \mathbf{x}\|}, \|\mathbf{x}_c - \mathbf{x}\|), \quad (1)$$

where $(\mathbf{x}_c - \mathbf{x})$ defines the viewing direction. We then compute the per-splat attributes as

$$\begin{aligned} o &= \text{MLP}_o(\mathbf{f}^*), & (\text{opacity}) \\ c &= \text{MLP}_c(\mathbf{f}^*), & (\text{color}) \\ r &= \text{MLP}_r(\mathbf{f}^*), & (\text{orientation}) \\ s^* &= \mathbf{s} \odot \text{sigmoid}(\text{MLP}_s(\mathbf{f}^*)), & (\text{scaling}) \end{aligned} \quad (2)$$

where $o \in \mathbb{R}$, $c \in \mathbb{R}^3$, $r \in \mathbb{R}^4$, and $s^* \in \mathbb{R}^3$ are the predicted opacity, color, rotation, and scaling, respectively, and \odot denotes element-wise multiplication. Generating scaling parameters s^* by relying solely on the MLP would cause instability and easily lead to training collapse. Thus, the parameter \mathbf{s} serves as a bound for the splat size that is scaled by the output from the MLP. The scaling matrix \mathbf{S} and rotation matrix \mathbf{R} defined by s^* and r reconstructs the covariance Σ of the splat:

$$\Sigma = \mathbf{R} \mathbf{S} \mathbf{S}^\top \mathbf{R}^\top. \quad (3)$$

The pixel-wise rasterization follows the α -blending in original 3DGS [18]. For each pixel $\mathbf{x}' \in \mathbb{R}^2$ in the 2D plane, the color $C(\mathbf{x}')$ is obtained by projecting all neural splats onto the image plane and compositing them along the ray by blending:

$$C(\mathbf{x}') = \sum_{i=1}^{N_{\text{ray}}} T_i o_i G(\mathbf{x}') \mathbf{c}_i, \quad T_i = \prod_{j=1}^{i-1} (1 - o_j G'(\mathbf{x}')), \quad (4)$$

where N_{ray} is the number of splats along the ray such that they are ordered by the distance to the camera center, and $G(\mathbf{x}')$ is the projected Gaussian weight:

$$G(\mathbf{x}') = \exp \left(-\frac{1}{2} (\mathbf{x}' - \boldsymbol{\mu}')^\top \boldsymbol{\Sigma}'^{-1} (\mathbf{x}' - \boldsymbol{\mu}') \right). \quad (5)$$

Here, the $\boldsymbol{\mu}' = \mathbf{J} \mathbf{W} \mathbf{x}$ and $\boldsymbol{\Sigma}' = \mathbf{J} \mathbf{W} \boldsymbol{\Sigma} \mathbf{J}^\top \mathbf{W}^\top$ are the splat coordinate and covariance after projection onto the 2D plane [21, 52], where \mathbf{J} denotes the Jacobian of projective transformation and \mathbf{W} is the view matrix. This parametrization in Smol-GS keeps geometry explicit and view effects compact, setting up the coordinate and feature compression modules described next.

3.2. Coordinate Compression: Occupancy-Octree Encoding

Many 3DGS compression methods avoid coordinate quantization due to the sensitivity of reconstruction to geometry. Our example in Fig. 4 shows that this precision requirement could be relaxed: 16-bit per-axis quantization yields an imperceptible quality drop. Therefore, inspired by point cloud geometry compression methods [6, 9, 37, 39], we use an octree structure to capture the occupancy of splats in 3D space such that the tree is built recursively.

We begin from the axis-aligned bounding box covering all splats and, at recursion $r = 1$, subdivide it into 8 equal sub-boxes. At each subsequent recursion, only *non-empty* boxes (those containing at least one splat) are subdivided again into 8 equal children. A box at depth $r \in \mathbb{N}$ has size $(\mathbf{x}_{\max} - \mathbf{x}_{\min})/2^r$. Each subdivision emits an 8-bit *occupancy byte* indicating which children are non-empty (1) or empty (0), with child order given by the Morton space-filling curve [30]. After R recursions, the resulting occupancy-octree explicitly represents the spatial layout of all splats (Fig. 5) such that the center of each leaf at depth R provides the quantized coordinate, with only one splat in each leaf.

Storing coordinates then reduces to recording the sequence of occupancy bytes for all non-empty internal nodes, plus the bounding box and depth R . Because these bytes are highly sparse (most nodes have few occupied children, see Sec. B.4), we apply Huffman coding [15] to entropy-compress them, yielding compact *lossless-within-grid* storage of coordinates relative to the chosen quantization grid.

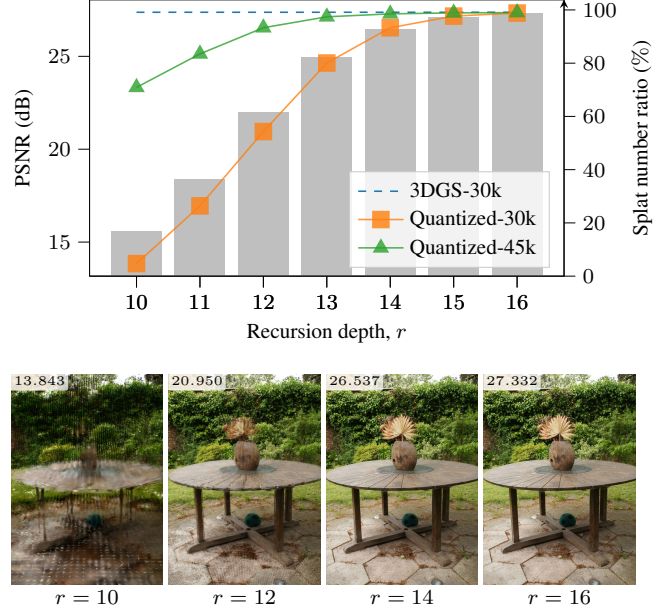


Figure 4. **Occupancy-octree depth vs. PSNR.** We experiment with quantizing the coordinates of a trained 3DGS-30k model to be the ‘Quantized-30k’ models. These models are finetuned as ‘Quantized-45k’ for an additional 15k iterations with quantized coordinates fixed. Top: Quantitative metrics (PSNR) and splat number ratio after quantization vs. quantization recursion on the *Garden* scene. Bottom: Qualitative results of Quantized-30k. Higher recursions yield better quality but keep more splats.

3.3. Splat-wise Feature Compression: Arithmetic Encoding

Each splat carries an abstract feature $\mathbf{f} \in \mathbb{R}^{n_f}$ encoding color, opacity, transformation, and material cues (see Sec. 3.1). In our setup, the features are low-dimensional and we choose $n_f = 8$ (see Sec. B.1 for discussion). Following HAC [4], we condition feature coding on spatial hash descriptors by predicting a distribution and a per-dimension step size with a tiny network MLP_h :

$$\boldsymbol{\mu}_f, \boldsymbol{\Sigma}_f, \Delta_f = \text{MLP}_h(\text{Hash}(\mathbf{x})), \quad (6)$$

where $\text{Hash}(\cdot)$ denotes the hash encoding function proposed in InstantNGP [31]. For better compression, the parameters of $\text{Hash}(\cdot)$ are quantized as binary. We then quantize the feature \mathbf{f} with the learned steps,

$$\hat{\mathbf{f}} = \Delta_f \odot \text{round}(\mathbf{f}/\Delta_f), \quad (7)$$

and assume the quantized features follow a Gaussian distribution of $\mathcal{N}(\mathbf{f}; \boldsymbol{\mu}_f, \boldsymbol{\Sigma}_f)$ (with diagonal $\boldsymbol{\Sigma}_f$). The negative log-likelihood (NLL) of the quantization bin provides a rate proxy:

$$\text{NLL}(\mathbf{f}) = -\log \int_{\hat{\mathbf{f}} - \Delta_f}^{\hat{\mathbf{f}} + \Delta_f} \mathcal{N}(\mathbf{f}'; \boldsymbol{\mu}_f, \boldsymbol{\Sigma}_f) d\mathbf{f}'. \quad (8)$$

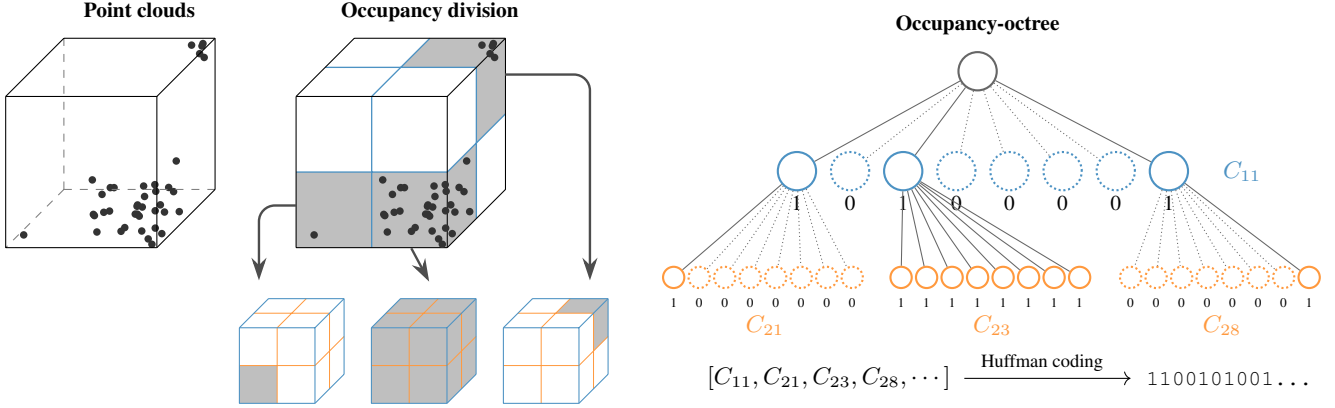


Figure 5. Occupancy-octree coordinate coding: Given a point cloud (left), we recursively divide the bounding box into eight sub-boxes. Only the non-empty sub-boxes (gray) are further divided. Each division is represented by an 8-bit binary code (1=non-empty, 0=empty). C_{ri} denotes the code of the j^{th} division at r^{th} recursion. The occupancy octree (right) is constructed by arranging all bits in a breadth-first manner. Finally, we apply Huffman coding to further compress the octree bits.

The NLL is the theoretical lower bound for the number of bits needed to encode the features. The average NLL over all N splats serves as the training loss to encourage reducing the storage for encoding the features:

$$\mathcal{L}_{\text{NLL}}(\mathbf{f}) = \frac{1}{N} \sum_{i=1}^N \text{NLL}(\mathbf{f}_i). \quad (9)$$

We use arithmetic coding [48] to compress both features \mathbf{f} and the scaling controller \mathbf{s} of the splats. The loss function of the scaling controller \mathbf{s} is defined similarly as Eq. (9) (i.e., $\mathcal{L}_{\text{NLL}}(\mathbf{s})$), and quantized as $\hat{\mathbf{s}}$ similarly as in Eq. (7).

3.4. Adaptive Density Control

To balance high-fidelity while having a sparse distribution of splats, Smol-GS employs an adaptive density control (ADC) strategy that adjusts the number of splats during training.

Initialization Following 3DGS [18], we initialize coordinates \mathbf{x} and scaling controllers \mathbf{s} from SfM point clouds [40]. Because SfM points are sparse and non-uniformly scattered, some regions require densification. The features \mathbf{f} are initialized randomly.

Densification Inspired by [27], splats with a high magnitude of the coordinate gradient are densified during training: a higher magnitude triggers the generation of more copies. We choose thresholds $\tau_{g_1} < \tau_{g_2} < \dots < \tau_{g_K}$ such that the splats whose coordinate's gradient magnitude is higher than τ_{g_m} will be split into 2^m new splats. The newly introduced splats inherit the features \mathbf{f} from their parent splat, while their coordinates are randomly sampled from a Gaussian $\mathcal{N}(\mathbf{x}, \Sigma)$, where \mathbf{x} and Σ are the coordinate and covariance of the parent splat, respectively. This process defines new splats and adds detail to under-represented regions of

the scene, improving reconstruction quality while rapidly increasing overall density.

Pruning During training, an individual splat is pruned when either its average opacity is less than the threshold τ_o , or if it remains consistently invisible.

Opacity Regularization To encourage sparsity in the splat distribution, we apply an ℓ_1 regularization loss on the opacity of all N splats during specific stages of training (see Sec. 3.5):

$$\mathcal{L}_o = \sum_{i=1}^N \text{MLP}_o(\mathbf{f}_i^*). \quad (10)$$

3.5. Training Pipeline for Smol-GS

We provide a consistent training pipeline, where Smol-GS is trained for 35k iterations with the following five stages: (1) *Warm-up stage* (0–0.5k): The splat coordinates \mathbf{x} and scaling controllers \mathbf{s} are initialized from SfM, and abstract features \mathbf{f} are randomly initialized. (2) *Densification stage* (0.5k–15k): The number of splats is controlled mutually by densification and pruning as described in Sec. 3.4. (3) *Compaction stage* (15k–20k): Both opacity regularization and pruning modules further reduce the number of splats. (4) *Feature compression stage* (20k–30k): Both features \mathbf{f} and scaling controllers \mathbf{s} of the splats are quantized via arithmetic encoding. (5) *Coordinate compression stage* (30k–35k): All splat coordinates are quantized and stored by the occupancy-octree technique. In Fig. 6, we provide training curves for an example scene (*Garden*), which gives an idea of the influence of the different stages.

Optimization Objective In stages (1)–(2), we optimize a photometric objective combining the norm-1 loss \mathcal{L}_1 and SSIM loss \mathcal{L}_s between the rendered image and the ground

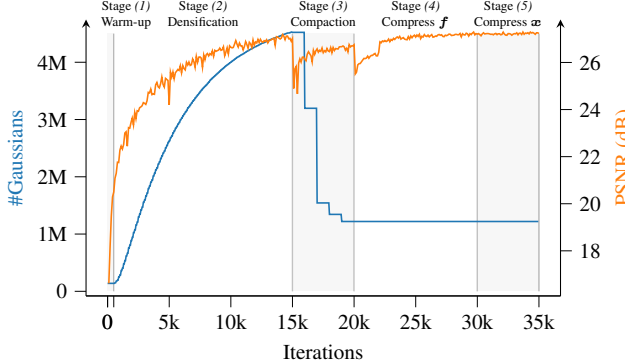


Figure 6. **Training curves over different stages:** We log the number of splats (left) and PSNR (right) over different stages of training, showing how the compaction and compression do not degrade the overall quality. The splat amount increases stably during densification (0.5k–15k), then decreases rapidly during compaction (15k–20k).

truth, the opacity regularization loss \mathcal{L}_o , and the quantization regularization losses of $\mathcal{L}_{\text{NLL}}(\mathbf{f}) + \mathcal{L}_{\text{NLL}}(\mathbf{s})$ such that

$$\mathcal{L} = (1 - \lambda_s)\mathcal{L}_1 + \lambda_s\mathcal{L}_s + \lambda_o\mathcal{L}_o + \lambda_q [\mathcal{L}_{\text{NLL}}(\mathbf{f}) + \mathcal{L}_{\text{NLL}}(\mathbf{s})]. \quad (11)$$

Here λ_s , λ_o , and λ_q are hyperparameters to control the optimization priorities of the SSIM loss, opacity regularization, and quantization regularization. The opacity regularization is only effective (*i.e.*, $\lambda_o > 0$) in the compaction stage (3), and the quantization regularization is only active (*i.e.*, $\lambda_q > 0$) during the compression stages of (4) and (5).

4. Experiments

We evaluate Smol-GS as a full 3DGS compression pipeline. Concretely, we demonstrate our rendering quality vs. model size both quantitatively and qualitatively under the 3DGS.zip survey benchmark setup. Additionally, we analyze storage size and the runtime impact of our tiny decoders and ablate central parts of our model.

Data Sets We benchmark our Smol-GS on standard real-world 3D reconstruction data sets: nine scenes from MIP-NERF 360 [2], two scenes from TANKS AND TEMPLES [20], and two scenes from DEEP BLENDING [12]. The training–testing split follows the original settings of 3DGS [18] and Mip-NeRF 360 [2]: Every 8th image is used for testing, and the rest are for training.

Evaluation Metrics The reconstruction quality is evaluated by three widely used metrics: the Peak Signal-to-Noise Ratio (PSNR), the Structural Similarity Index Measure (SSIM), and the Learned Perceptual Image Patch Similarity (LPIPS). PSNR computes the signal preservation level via pixel-wise mean squared error, SSIM measures the statistical structural similarity, and LPIPS estimates the human perceptual difference based on features extracted from pre-trained neural

networks [53]. The compression ratio is measured by the final model size in megabytes (MB), which includes all components: coordinates, abstract features, scaling controllers, and MLP parameters.

Implementation Details Smol-GS is implemented in PyTorch [35] using the Inria 3DGS repository [18] as a starting point. Parameters of the model are trained using the Adam optimizer [19]. The loss coefficients in Eq. (11) are set to $\lambda_s = 0.2$, and $\lambda_q = 10^{-3}$. The thresholds for densification are set to $\tau_{g_k} = 2^k \times 10^{-4}$ where $k = 1, 2, \dots, 5$, and the opacity pruning threshold is $\tau_o = 5 \times 10^{-3}$. We fix the feature \mathbf{f} dimensionality to $n_f = 8$, and all scenes are discretized with $R = 16$ recursions for coordinate compression. Additional implementation details, including learning rate (lr) values, lr schedules, and MLP architectures, are provided in Sec. A.

Smol-GS is stored as multiple components: (*i*) occupancy-octree data as bit strings to represent quantized coordinates $\hat{\mathbf{x}}$, (*ii*) binary arithmetic codes representing compressed features $\hat{\mathbf{f}}$ and scaling controllers $\hat{\mathbf{s}}$, (*iii*) MLP architecture/weights (MLP _{α} , MLP _{c} , MLP _{s} , MLP _{r}), and (*iv*) additional metadata (*i.e.*, the lower and upper bounds of the scene, number of recursions R). The total Smol-GS size reported in this paper is the size of a single zip file containing all these four components (following the 3DGS.zip survey [1]). Table 2 represents the size of each component in Smol-GS for the *Garden* scene. The reported reconstruction quality metrics represent the average value computed between the ground-truth images (from test sets) and the rendered images from the compressed model.

Smol-GS variants We include three variants of Smol-GS (base, small, tiny) in the results with different compaction hyperparameters λ_o (base: $\lambda_o = 2 \times 10^{-7}$, small: $\lambda_o = 3 \times 10^{-7}$, tiny: $\lambda_o = 4 \times 10^{-7}$).

Baselines We compare Smol-GS with the most efficient and recent 3DGS compression methods of Compact3DGS [23], SOG [29], Reducing3DGS [34], Compressed3DGS [33], CompGS [32], HAC [4], ContextGS [46], HEMGS [25], and HAC++ [5]. We also provide the original vanilla 3DGS results as the prototype baseline.

4.1. Results on 3DGS Compression Benchmarks

Quantitative Results We compare Smol-GS with the baselines on three benchmark data sets using the four evaluation metrics mentioned earlier. The quantitative results are summarized in Table 1 and Fig. 7. The quantitative results of the baselines are collected from the 3DGS.zip compression survey [1]. In Table 1, Smol-GS achieves the highest compression ratio of all baselines with a considerable margin, reducing the model size by about 150 \times compared to vanilla 3DGS without any substantial quality drop (no drop on PSNR). In the scatter plots in Fig. 7, Smol-GS outperforms all current state-of-the-art baselines in terms of compression ratio

Table 1. **Smol-GS provides excellent quality-size trade-off:** We report PSNR/SSIM/LPIPS and the *total model size in MBs* following the 3DGS.zip survey benchmark [1]. Across MIP-NERF 360, TANKS AND TEMPLES, and DEEP BLENDING, Smol-GS has the smallest sizes while maintaining quality similar to the strongest methods, indicating a better rate-distortion trade-off. See also Fig. 7.

Methods	MIP-NERF 360				TANKS AND TEMPLES				DEEP BLENDING			
	PSNR↑	SSIM↑	LPIPS↓	Size↓	PSNR↑	SSIM↑	LPIPS↓	Size↓	PSNR↑	SSIM↑	LPIPS↓	Size↓
3DGS-30K [18]	27.21	0.815	0.214	734	23.14	0.841	0.183	411	29.41	0.903	0.243	676
Compact3DGS [23]	27.08	0.798	0.247	48.8	23.32	0.831	0.201	39.4	29.79	0.901	0.258	43.2
SOG [29]	27.08	0.799	0.230	40.28	23.56	0.837	0.186	22.78	29.26	0.894	0.268	17.74
Reducing3DGS [34]	27.10	0.809	0.226	29	23.57	0.840	0.188	14	29.63	0.902	0.249	18
Compressed3D [33]	26.98	0.801	0.238	28.8	23.32	0.832	0.194	17.28	29.38	0.898	0.253	25.3
CompGS [32]	27.03	0.804	0.243	18	23.39	0.836	0.200	12	29.90	0.906	0.252	12
HAC [4]	27.53	0.807	0.238	16.01	24.04	0.846	0.187	8.494	29.98	0.902	0.269	4.561
ContextGS [46]	27.62	0.808	0.237	13.3	24.12	0.849	0.186	9.902	30.09	0.907	0.265	3.655
HEMGS [25]	27.75	0.806	0.248	12.54	24.42	0.848	0.192	6.034	30.24	0.908	0.266	2.993
HAC++ [5]	27.60	0.803	0.253	8.742	24.22	0.849	0.190	5.427	30.16	0.907	0.266	3.051
Smol-GS-base	27.51	0.806	0.242	6.44	23.98	0.842	0.191	5.525	30.02	0.907	0.252	3.345
Smol-GS-small	27.29	0.798	0.260	4.746	23.83	0.838	0.200	4.455	29.90	0.905	0.256	2.599

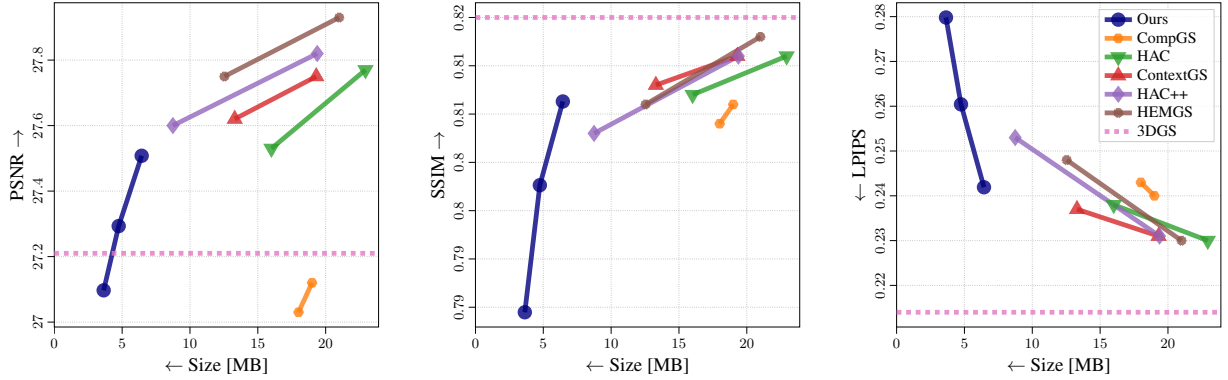


Figure 7. **Comparison of top methods on MIP-NERF 360.** Each point is a method; the *x*-axis is total model size in MBs (smaller is better) and the *y*-axis reports PSNR/SSIM (higher is better) or LPIPS (lower is better). Smol-GS (tiny-small-base) consistently lies on or beyond the Pareto frontier, achieving markedly smaller sizes at comparable quality to strong baselines collected via the 3DGS.zip benchmark. See Fig. A13 in the Appendix for results on TANKS AND TEMPLES and DEEP BLENDING.

while maintaining adequate reconstruction quality. We include further scatter plots for TANKS AND TEMPLES and DEEP BLENDING in Fig. A13 in the Appendix.

Qualitative Results Fig. 2 (MIP-NERF 360) and Fig. 8 (TANKS AND TEMPLES and DEEP BLENDING) show qualitative comparison of Smol-GS, vanilla 3DGS, and the ground-truth test views for different scenes. We highlight specific regions by providing zoomed-in views for better subjective comparison. The rendered test views show that Smol-GS is capable of reconstructing scene details with high-fidelity and preserving sharp edges. Especially, for challenging objectives such as the stainless steel bowl in the *Counter* scene, the glass bottle in the *Room* scene, and the white wall in the *Bonsai* scene, Smol-GS clearly recovers the visual effects of reflection and transparency better than vanilla 3DGS. We link these visual improvements to the neural representation of abstract splats, which is capable to learn

the optical properties and material cues of different surfaces adaptively. This representation is substantially more efficient in storing view-dependent cues compared to the expensive-to-store 3rd degree spherical harmonic coefficients in 3DGS.

Storage Size The required disk space for storing each model component in Smol-GS (we present this for the -base variant) is summarized in Table 2. The splat-wise features f take the majority of the space, while storing the coordinates x is very efficient thanks to the proposed occupancy-octree encoding.

Table 2. The size of each component of Smol-GS-base (in MB), value reported averaged over all scenes.

Model size (MB)	Total	x	f	s	MLPs	Others
MIP-NERF 360	6.440	1.412	3.245	1.634	0.134	0.014
DEEP BLENDING	3.345	0.816	1.451	0.942	0.127	0.010
TANKS AND TEMPLES	5.525	0.931	2.889	1.580	0.113	0.013



Figure 8. **Qualitative results on the TANKS AND TEMPLES and DEEP BLENDING data sets.** Smol-GS has fewer artefacts and better preservation of scene details under challenging lighting and materials. The learned splat features in Smol-GS capture view-dependent and material cues more compactly than SH, aligning with its smaller size in MBs and competitive metrics in Table 1.

Table 3. Encoding time of each component of Smol-GS-base (in seconds), values reported averaged over all scenes.

Encoding time (s)	Total	x	f	s	MLPs
MIP-NERF 360	2.361	0.179	1.326	0.744	0.020
DEEP BLENDING	1.261	0.112	0.651	0.443	0.016
TANKS AND TEMPLES	2.040	0.118	1.180	0.679	0.015

Table 4. Decoding time of each component of Smol-GS-base (in seconds), values reported averaged over all scenes.

Decoding time (s)	Total	x	f	s	MLPs
MIP-NERF 360	3.565	0.153	1.956	1.428	0.017
DEEP BLENDING	1.823	0.090	0.874	0.836	0.017
TANKS AND TEMPLES	3.147	0.097	1.709	1.315	0.016

The MLP parameters only take a negligible portion of the total size due to their tiny architecture. Compared to other methods like HAC++, we save space by storing less data per splat and by allowing the tiny MLPs to efficiently pack the required cues into the low-dimensional features.

Training Time, Encoding/Decoding Timings, and Rendering Speed The training time of the Smol-GS-base model is around 32 minutes per scene on average. The encoding and decoding timings of Smol-GS-base for the benchmark data sets are presented in Tables 3 and 4, respectively. The fast encoding and decoding speed ensures the practicality of Smol-GS in storage and transmission scenarios. The average rendering speed of Smol-GS-base model is 245.7 fps (MIP-NERF 360: 215.1 fps, DEEP BLENDING: 405.5 fps, and TANKS AND TEMPLES: 223.4 fps). The timings were measured on NVIDIA H200 GPUs (see Sec. A.1 for details).

4.2. Ablations on Model Hyperparameters

We conduct different ablation studies to evaluate the impact of each hyperparameter in Smol-GS, including the number of recursions in occupancy-octree encoding of coordinates (see Fig. A9), the feature dimension n_f (see Fig. A10), the compaction strength λ_o (see Fig. A11), and the arithmetic encoding strength λ_q (see Fig. A12). More detailed results are listed at Sec. B.1.

5. Discussion and Conclusion

We introduced Smol-GS, a compact 3DGS representation that keeps geometry *explicit* and efficiently packed and abstracts view-dependent appearance into low-dimensional, arithmetically coded splat features. Smol-GS achieves the highest compression ratio among existing baseline models, maintains competitive reconstruction quality, and preserves primitive structure—thus providing compatibility to various 3DGS applications. The compact storage and efficient decoding also facilitate real-time rendering and transmission of 3D scenes in resource-constrained environments. Extensive experiments on standard 3D reconstruction data sets validate the effectiveness of Smol-GS thorough quantitative and qualitative views.

The discrete representations of splat features could serve as 3D information tokens, enabling possibilities for combination with other learning modalities and language models. The discrete primitive distribution can potentially be improved by depth estimation techniques. The octree hierarchy implies relations among splats, which can improve representation by leveraging prior knowledge of the geometry.

References

[1] Milena T Bagdasarian, Paul Knoll, Y Li, Florian Barthel, Anna Hilsmann, Peter Eisert, and Wieland Morgenstern. 3DGs.zip: A survey on 3D Gaussian splatting compression methods. In *Computer Graphics Forum*, page e70078. Wiley Online Library, 2025. 6, 7

[2] Jonathan T. Barron, Ben Mildenhall, Dor Verbin, Pratul P. Srinivasan, and Peter Hedman. Mip-NeRF 360: Unbounded anti-aliased neural radiance fields. In *Proceedings of the IEEE/CVF Conference on Computer Vision and Pattern Recognition (CVPR)*, pages 5470–5479, 2022. 6

[3] Yiwen Chen, Zilong Chen, Chi Zhang, Feng Wang, Xiaofeng Yang, Yikai Wang, Zhongang Cai, Lei Yang, Huaping Liu, and Guosheng Lin. GaussianEditor: Swift and controllable 3D editing with Gaussian splatting. In *Proceedings of the IEEE/CVF conference on Computer Vision and Pattern Recognition (CVPR)*, pages 21476–21485, 2024. 2

[4] Yihang Chen, Qianyi Wu, Weiyao Lin, Mehrtash Harandi, and Jianfei Cai. HAC: Hash-grid assisted context for 3D Gaussian splatting compression. In *Proceedings of the European Conference on Computer Vision (ECCV)*, pages 422–438. Springer, 2024. 1, 4, 6, 7

[5] Yihang Chen, Qianyi Wu, Weiyao Lin, Mehrtash Harandi, and Jianfei Cai. HAC++: Towards 100x compression of 3D Gaussian splatting. *arXiv preprint arXiv:2501.12255*, 2025. 1, 2, 6, 7

[6] Mingyue Cui, Junhua Long, Mingjian Feng, Boyang Li, and Huang Kai. Octformer: Efficient octree-based transformer for point cloud compression with local enhancement. In *Proceedings of the AAAI Conference on Artificial Intelligence*, pages 470–478, 2023. 3, 4

[7] Zhiwen Fan, Kevin Wang, Kairun Wen, Zehao Zhu, Dejia Xu, and Zhangyang Wang. LightGaussian: Unbounded 3D Gaussian compression with 15x reduction and 200+ fps. In *Advances in Neural Information Processing Systems (NeurIPS)*, pages 140138–140158. Curran Associates, Inc., 2024. 1, 2

[8] Guangchi Fang and Bing Wang. Mini-splatting: Representing scenes with a constrained number of Gaussians. In *Proceedings of the European Conference on Computer Vision (ECCV)*, pages 165–181. Springer, 2024. 1, 2

[9] Chunyang Fu, Ge Li, Rui Song, Wei Gao, and Shan Liu. Octtattention: Octree-based large-scale contexts model for point cloud compression. In *Proceedings of the AAAI conference on artificial intelligence*, pages 625–633, 2022. 3, 4

[10] Allen Gersho and Robert M Gray. *Vector Quantization and Signal Compression*. Springer Science & Business Media, 2012. 2

[11] Sharath Girish, Kamal Gupta, and Abhinav Shrivastava. EA-GLES: Efficient accelerated 3D Gaussians with lightweight encodings. In *Proceedings of the European Conference on Computer Vision (ECCV)*, pages 54–71. Springer, 2024. 1

[12] Peter Hedman, Julien Philip, True Price, Jan-Michael Frahm, George Drettakis, and Gabriel Brostow. Deep blending for free-viewpoint image-based rendering. *ACM Transactions on Graphics (ToG)*, 37(6), 2018. 6

[13] Jiarui Hu, Xianhao Chen, Boyin Feng, Guanglin Li, Liangjing Yang, Hujun Bao, Guofeng Zhang, and Zhaopeng Cui. CG-SLAM: Efficient dense RGB-D slam in a consistent uncertainty-aware 3D Gaussian field. In *Proceedings of the European Conference on Computer Vision (ECCV)*, pages 93–112. Springer, 2024. 2

[14] Huajian Huang, Longwei Li, Hui Cheng, and Sai-Kit Yeung. Photo-SLAM: Real-time simultaneous localization and photo-realistic mapping for monocular stereo and RGB-D cameras. In *Proceedings of the IEEE/CVF Conference on Computer Vision and Pattern Recognition*, pages 21584–21593, 2024. 2

[15] David A Huffman. A method for the construction of minimum-redundancy codes. *Proceedings of the IRE*, 40(9):1098–1101, 2007. 3, 4

[16] Ying Jiang, Chang Yu, Tianyi Xie, Xuan Li, Yutao Feng, Huamin Wang, Minchen Li, Henry Lau, Feng Gao, Yin Yang, and Jiang Chenfanfu. VR-GS: A physical dynamics-aware interactive Gaussian splatting system in virtual reality. In *ACM SIGGRAPH (Conference Paper Track)*, 2024. 2

[17] Nikhil Keetha, Jay Karhade, Krishna Murthy Jatavallabhula, Gengshan Yang, Sebastian Scherer, Deva Ramanan, and Jonathon Luiten. SplaTAM: Splat track & map 3D Gaussians for dense RGB-D SLAM. In *Proceedings of the IEEE/CVF Conference on Computer Vision and Pattern Recognition (CVPR)*, pages 21357–21366, 2024. 2

[18] Bernhard Kerbl, Georgios Kopanas, Thomas Leimkühler, and George Drettakis. 3D Gaussian splatting for real-time radiance field rendering. *ACM Transactions on Graphics (ToG)*, 42(4), 2023. 1, 4, 5, 6, 7

[19] Diederik P Kingma. Adam: A method for stochastic optimization. *arXiv preprint arXiv:1412.6980*, 2014. 6, 1

[20] Arno Knapitsch, Jaesik Park, Qian-Yi Zhou, and Vladlen Koltun. Tanks and temples: Benchmarking large-scale scene reconstruction. *ACM Transactions on Graphics (ToG)*, 36(4), 2017. 6

[21] Georgios Kopanas, Julien Philip, Thomas Leimkühler, and George Drettakis. Point-based neural rendering with per-view optimization. In *Computer Graphics Forum*, pages 29–43. Wiley Online Library, 2021. 4

[22] Christoph Lassner and Michael Zollhofer. Pulsar: Efficient sphere-based neural rendering. In *Proceedings of the IEEE/CVF conference on computer vision and pattern recognition*, pages 1440–1449, 2021. 1

[23] Joo Chan Lee, Daniel Rho, Xiangyu Sun, Jong Hwan Ko, and Eunbyung Park. Compact 3D Gaussian representation for radiance field. In *Proceedings of the IEEE/CVF Conference on Computer Vision and Pattern Recognition (CVPR)*, pages 21719–21728, 2024. 1, 2, 6, 7

[24] Yoseph Linde, Andres Buzo, and Robert Gray. An algorithm for vector quantizer design. *IEEE Transactions on Communications*, 28(1):84–95, 2003. 2

[25] Lei Liu, Zhenghao Chen, Wei Jiang, Wei Wang, and Dong Xu. HEMGS: A hybrid entropy model for 3D Gaussian splatting data compression. *arXiv preprint arXiv:2411.18473*, 2024. 1, 2, 6, 7

[26] Stuart Lloyd. Least squares quantization in pcm. *IEEE Transactions on Information Theory*, 28(2):129–137, 1982. 2

[27] Tao Lu, Mulin Yu, Lining Xu, Yuanbo Xiangli, Limin Wang, Dahua Lin, and Bo Dai. Scaffold-GS: Structured

3D Gaussians for view-adaptive rendering. In *Proceedings of the IEEE/CVF Conference on Computer Vision and Pattern Recognition (CVPR)*, pages 20654–20664, 2024. 1, 2, 5

[28] Saswat Subhajyoti Mallick, Rahul Goel, Bernhard Kerbl, Markus Steinberger, Francisco Vicente Carrasco, and Fernando De La Torre. Taming 3DGS: High-quality radiance fields with limited resources. In *SIGGRAPH Asia 2024 Conference Papers*, pages 1–11, 2024. 1, 2

[29] Wieland Morgenstern, Florian Barthel, Anna Hilsmann, and Peter Eisert. Compact 3D scene representation via self-organizing Gaussian grids. In *Proceedings of the European Conference on Computer Vision (ECCV)*, pages 18–34. Springer, 2024. 1, 6, 7

[30] Guy M Morton. *A Computer Oriented Geodetic Data Base and a New Technique in File Sequencing*. International Business Machines Company, 1966. 4

[31] Thomas Müller, Alex Evans, Christoph Schied, and Alexander Keller. Instant neural graphics primitives with a multiresolution hash encoding. *ACM Transactions on Graphics (ToG)*, 41(4):1–15, 2022. 4

[32] KL Navaneet, Kossar Pourahmadi Meibodi, Soroush Abbasi Koohpayegani, and Hamed Pirsavash. CompGS: Smaller and faster Gaussian splatting with vector quantization. In *Proceedings of the European Conference on Computer Vision (ECCV)*, pages 330–349. Springer, 2024. 1, 2, 6, 7

[33] Simon Niedermayr, Josef Stumpfegger, and Rüdiger Westermann. Compressed 3D Gaussian splatting for accelerated novel view synthesis. In *Proceedings of the IEEE/CVF Conference on Computer Vision and Pattern Recognition (CVPR)*, pages 10349–10358, 2024. 6, 7

[34] Panagiotis Papantonakis, Georgios Kopanas, Bernhard Kerbl, Alexandre Lanvin, and George Drettakis. Reducing the memory footprint of 3D Gaussian splatting. *Proceedings of the ACM on Computer Graphics and Interactive Techniques*, 7(1):1–17, 2024. 1, 2, 6, 7

[35] Adam Paszke, Sam Gross, Francisco Massa, Adam Lerer, James Bradbury, Gregory Chanan, Trevor Killeen, Zeming Lin, Natalia Gimelshein, Luca Antiga, et al. Pytorch: An imperative style, high-performance deep learning library. *Advances in Neural Information Processing Systems (NeurIPS)*, 32, 2019. 6, 1

[36] Stéphane Pateux, Matthieu Gendrin, Luce Morin, Théo Ladune, and Xiaoran Jiang. BOGausS: Better optimized Gaussian splatting. *arXiv preprint arXiv:2504.01844*, 2025. 1, 2

[37] Zizheng Que, Guo Lu, and Dong Xu. Voxelcontext-net: An octree based framework for point cloud compression. In *Proceedings of the IEEE/CVF Conference on Computer Vision and Pattern Recognition*, pages 6042–6051, 2021. 3, 4

[38] Kerui Ren, Lihan Jiang, Tao Lu, Mulin Yu, Linning Xu, Zhangkai Ni, and Bo Dai. Octree-GS: Towards consistent real-time rendering with lod-structured 3D Gaussians. *arXiv preprint arXiv:2403.17898*, 2024. 1, 2

[39] Ruwen Schnabel and Reinhard Klein. Octree-based point-cloud compression. In *Proceedings of the 3rd Eurographics / IEEE VGTC Conference on Point-Based Graphics*, page 111–121, Goslar, DEU, 2006. Eurographics Association. 2, 3, 4

[40] Johannes L Schonberger and Jan-Michael Frahm. Structure-from-motion revisited. In *Proceedings of the IEEE conference on Computer Vision and Pattern Recognition (CVPR)*, pages 4104–4113, 2016. 2, 5

[41] Ruizhi Shao, Jingxiang Sun, Cheng Peng, Zerong Zheng, Boyao Zhou, Hongwen Zhang, and Yebin Liu. Control4D: Efficient 4D portrait editing with text. In *Proceedings of the IEEE/CVF Conference on Computer Vision and Pattern Recognition*, pages 4556–4567, 2024. 2

[42] Jiaxiang Tang, Jiawei Ren, Hang Zhou, Ziwei Liu, and Gang Zeng. DreamGaussian: Generative Gaussian splatting for efficient 3D content creation. *arXiv preprint arXiv:2309.16653*, 2023. 2

[43] Mohammad Hassan Vali and Tom Bäckström. Stochastic optimization of vector quantization methods in application to speech and image processing. In *International Conference on Acoustics, Speech and Signal Processing (ICASSP)*, pages 1–5, 2023. 2

[44] Aaron Van Den Oord, Oriol Vinyals, and Koray Kavukcuoglu. Neural discrete representation learning. In *Advances in Neural Information Processing Systems 30 (NIPS)*. Curran Associates, Inc., 2017. 2

[45] Haishan Wang, Mohammad Hassan Vali, and Arno Solin. Compressing 3D Gaussian splatting by noise-substituted vector quantization. In *Scandinavian Conference on Image Analysis (SCIA)*, pages 338–352. Springer, 2025. 1

[46] Yufei Wang, Zhihao Li, Lanqing Guo, Wenhan Yang, Alex Kot, and Bihai Wen. ContextGS: Compact 3D Gaussian splatting with anchor level context model. In *Advances in Neural Information Processing Systems (NeurIPS)*, pages 51532–51551. Curran Associates, Inc., 2024. 1, 2, 6, 7

[47] Lee Alan Westover. *Splatting: A Parallel, Feed-Forward Volume Rendering Algorithm*. The University of North Carolina at Chapel Hill, 1991. 2

[48] Ian H Witten, Radford M Neal, and John G Cleary. Arithmetic coding for data compression. *Communications of the ACM*, 30(6):520–540, 1987. 5

[49] Jing Wu, Jia-Wang Bian, Xinghui Li, Guangrun Wang, Ian Reid, Philip Torr, and Victor Adrian Prisacariu. GaussCtrl: Multi-view consistent text-driven 3D Gaussian splatting editing. In *Proceedings of the European Conference on Computer Vision (ECCV)*, pages 55–71. Springer, 2024. 2

[50] Chi Yan, Delin Qu, Dan Xu, Bin Zhao, Zhigang Wang, Dong Wang, and Xuelong Li. GS-SLAM: Dense visual SLAM with 3D Gaussian splatting. In *Proceedings of the IEEE/CVF Conference on Computer Vision and Pattern Recognition (CVPR)*, pages 19595–19604, 2024. 2

[51] Vickie Ye, Rui long Li, Justin Kerr, Matias Turkulainen, Brent Yi, Zhuoyang Pan, Otto Seiskari, Jianbo Ye, Jeffrey Hu, Matthew Tancik, et al. gsplat: An open-source library for Gaussian splatting. *Journal of Machine Learning Research (JMLR)*, 26(34):1–17, 2025. 1

[52] Wang Yifan, Felice Serena, Shihao Wu, Cengiz Öztireli, and Olga Sorkine-Hornung. Differentiable surface splatting for point-based geometry processing. *ACM Transactions on Graphics (ToG)*, 38(6):1–14, 2019. 4

[53] Richard Zhang, Phillip Isola, Alexei A. Efros, Eli Shechtman, and Oliver Wang. The unreasonable effectiveness of

deep features as a perceptual metric. In *Proceedings of the IEEE Conference on Computer Vision and Pattern Recognition (CVPR)*, 2018. 6

[54] Tianyuan Zhang, Hong-Xing Yu, Rundi Wu, Brandon Y Feng, Changxi Zheng, Noah Snavely, Jiajun Wu, and William T Freeman. PhysDreamer: Physics-based interaction with 3d objects via video generation. In *Proceedings of the European Conference on Computer Vision (ECCV)*, pages 388–406. Springer, 2024. 2

[55] Yangming Zhang, Wenqi Jia, Wei Niu, and Miao Yin. GaussianSpa: An “optimizing-sparsifying” simplification framework for compact and high-quality 3D Gaussian splatting. In *Proceedings of the IEEE/CVF Conference on Computer Vision and Pattern Recognition (CVPR)*, pages 26673–26682, 2025. 1, 2

[56] Jingyu Zhuang, Di Kang, Yan-Pei Cao, Guanbin Li, Liang Lin, and Ying Shan. Tip-editor: An accurate 3D editor following both text-prompts and image-prompts. *ACM Transactions on Graphics (ToG)*, 43(4):1–12, 2024. 2

[57] Wojciech Zelenka, Timur Bagautdinov, Shunsuke Saito, Michael Zollhöfer, Justus Thies, and Javier Romero. Drivable 3D Gaussian avatars. In *International Conference on 3D Vision (3DV)*, pages 979–990. IEEE, 2025. 2

[58] Matthias Zwicker, Hanspeter Pfister, Jeroen Van Baar, and Markus Gross. Ewa splatting. *IEEE Transactions on Visualization and Computer Graphics*, 8(3):223–238, 2002. 2

Smol-GS: Compact Representations for Abstract 3D Gaussian Splatting

Supplementary Material

A. Implementation Details

A.1. Hardware and Software

Our experiments are conducted on NVIDIA H200 GPUs with 141 GB memory. The codes are implemented in Python (python=2.11) using the PyTorch framework (version 2.4.1) [35] with CUDA 12.4. The Gaussian rasterization module is built on top of the Inria 3DGS repository [18]. The arithmetic coding and hash encoding functions modules are built upon the implementations from HAC [4].

A.2. Optimization Details

Learning rates and schedulers The model parameters are optimized using the Adam optimizer [19]. We use an exponential decay scheduler on learning rates of abstract features f , coordinates x , all MLPs ($MLP_o, MLP_c, MLP_r, MLP_s, MLP_h$), and the hash encoder $\text{Hash}(\cdot)$. For each parameter, the learning rate η_i at iteration i is defined as

$$\eta_i = \exp((1 - t) \log(\eta_0) + t \log(\eta_{\text{end}})), \quad (12)$$

where $t = \text{clamp}\left(\frac{i}{I}, \min = 0, \max = 1\right)$,

here I is the maximum iteration for learning rate scheduler, η_0 and η_{end} are the initial and final learning rates, respectively. We use $I = 30000$, and the details of η_0 and η_{end} for different model parameters are shown in Table A5.

A.3. Adaptive Density Control Settings

The *Densification stage* (0.5k–15k iterations) starts at $i_{\text{start}} = 500$ and end at $i_{\text{end}} = 15000$, and the pruning threshold on opacity is set to

$$\tau_o = \lambda(5 \times 10^{-3}) + (1 - \lambda)10^{-4}, \quad (13)$$

where $\lambda = (i - i_{\text{start}})/(i_{\text{end}} - i_{\text{start}})$. (14)

The densification threshold on the magnitude of coordinate gradients is defined as $\tau_{g_k} = 2^k \times 10^{-4}$ where $k = 1, 2, \dots, 5$. During the *Compaction stage* (15k - 20k iterations), there is no densification module applied, and the pruning threshold on opacity is set to $\tau_o = 5 \times 10^{-3}$.

A.4. Model Hyperparameters

The feature dimension is fixed to $n_f = 8$, and the number of recursions of occupancy-octree for coordinate compression is set to $R = 16$.

MLP architectures The MLP architecture metadata, including the input dim., output dim., hidden dim., layers,

normalization layer type, and activation layer type, is summarized in Table A6. The input dimensions of $MLP_o, MLP_c, MLP_r, MLP_s$ are $n_f + 4$, which is defined by the concatenation of the abstract feature f (dimension $n_f = 8$), the 3D viewing direction, and the viewing distance.

Hash encoder The hash encoder $\text{Hash}(\cdot)$ contains both 2D and 3D hash tables, with size of 2^{15} and 2^{13} , respectively. There are 4-dimensional features per level. The resolution lists of 2D and 3D hash table are defined as (130, 258, 514, 1026) and (18, 24, 33, 44, 59, 80, 108, 148, 201, 275, 376, 514).

Regularization hyperparameters For the default settings (Smol-GS-base), the regularization hyperparameters are set as $\lambda_o = 2 \times 10^{-7}$, $\lambda_q = 1 \times 10^{-3}$ and λ_s , where λ_o, λ_q and λ_s denote the weights for opacity regularization, quantization regularization, and SSIM-loss regularization, respectively.

B. Additional Experiments

In this section, we provide ablation studies on different model hyperparameters and optimization hyperparameters in Sec. B.1, additional quantitative results in Sec. B.2, additional qualitative results in Sec. B.3, occupancy-octree analysis in Sec. B.4, encoding and decoding time on each model component per scene in Sec. B.5, and the interpretation of learned abstract features in Sec. B.6.

B.1. Ablation Studies

We conduct ablation studies on four different hyperparameters in Smol-GS, including feature dimension n_f , recursion level R , the loss weights on opacity regularization λ_o , and quantization regularization λ_q .

Recursion level R The value of the recursion level R controls the compression ratio of splat coordinates. The ablation experiment on recursion levels R is presented in Table A7 and Fig. A9, the value of R is set to $\{13, 14, 15, 16, 17\}$ in the experiments. Larger R requires more storage memory of coordinate in a linear manner, and leads to better reconstruction quality. Recursion level $R = 16$ provides a good trade-off between compression ratio and reconstruction quality. Different datasets might prefer different R for the best trade-off due to the different space ranges, e.g., TANKS AND TEMPLES prefers $R = 17$.

Feature dimension n_f The value of n_f controls the dimensionality of abstract features. The ablation experiment on feature dimension n_f is presented in Table A8 and Fig. A10, the value of n_f is set to $\{4, 6, 8, 16, 32\}$ in the experiments.

Table A5. **Learning schedulers** of model parameters, here η_0 and η_{end} denote the initial and final learning rates. And the learning rate follows an exponential decay schedule defined in Eq. (12).

	\mathbf{x}	\mathbf{f}	MLP_o	MLP_c	MLP_r	MLP_s	MLP_h	Hash
η_0	0.0002	0.0075	0.002	0.008	0.004	0.004	0.005	0.005
η_{end}	1.6×10^{-6}	0.0075	2×10^{-5}	5×10^{-5}	0.004	0.004	1×10^{-5}	1×10^{-5}

Table A6. **Details of the MLP structures** in Smol-GS. here n_f denotes the feature dimension

	Input Dim	Layers	Hidden Dim	Normalization	Output Dim	Activation
MLP_o	$n_f + 4$	3	128	ReLU	1	$\tanh(\cdot)$
MLP_c	$n_f + 4$	3	128	ReLU	3	$\text{sigmoid}(\cdot)$
MLP_r	$n_f + 4$	3	128	ReLU	4	None
MLP_s	$n_f + 4$	3	128	ReLU	3	None
MLP_h	96	3	128	ReLU	$8 + 2n_f$	None

Table A7. **Ablation study on recursion level R** of occupancy-octree encoding. MIP-NERF 360 and DEEP BLENDING saturate around $R = 16$, while TANKS AND TEMPLES still improves at $R = 17$.

Recursion Level	MIP-NERF 360				TANKS AND TEMPLES				DEEP BLENDING			
	PSNR↑	SSIM↑	LPIPS↓	Size↓	PSNR↑	SSIM↑	LPIPS↓	Size↓	PSNR↑	SSIM↑	LPIPS↓	Size↓
$R = 13$	26.38	0.747	0.301	4.689	22.19	0.747	0.314	2.456	29.58	0.896	0.269	2.748
$R = 14$	27.14	0.785	0.263	5.628	23.36	0.808	0.239	3.934	29.82	0.902	0.260	2.948
$R = 15$	27.42	0.800	0.248	6.145	23.82	0.834	0.203	4.742	29.68	0.900	0.265	3.17
$R = 16$	27.56	0.806	0.241	6.533	23.90	0.840	0.192	5.31	29.91	0.906	0.252	3.431
$R = 17$	27.56	0.808	0.241	6.765	24.06	0.848	0.185	5.608	29.95	0.906	0.251	3.675

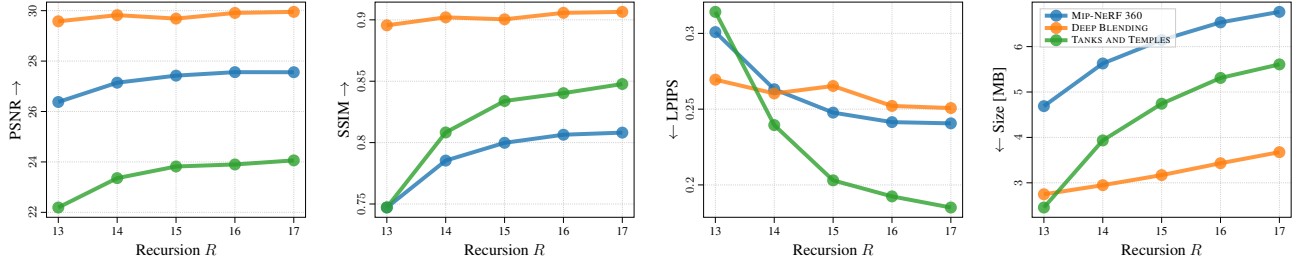


Figure A9. **Ablation study on recursion level R** of occupancy-octree encoding. In each subfigure, the x -axis represents different recursion level R , and the y -axis represents the corresponding metric values: PSNR, SSIM, LPIPS, size (in MBs).

Larger n_f requires more storage space for features, while improving the reconstruction quality. We choose feature dimension $n_f = 8$ for compact storage and competitive reconstruction quality.

Opacity regularization λ_o The value of λ_o controls the strength of opacity regularization. The ablation experiment on opacity regularization strength λ_o is presented in Table A9 and Fig. A11, the value of λ_o is set to $\{1 \times 10^{-7}, 2 \times 10^{-7}, 3 \times 10^{-7}, 4 \times 10^{-7}, 5 \times 10^{-7}\}$ in the experiments. The larger λ_o encourages the model to use fewer splats to represent the scene, resulting in worse reconstruction quality but smaller storage size. And $\lambda_o \in [2 \times 10^{-7}, 4 \times 10^{-7}]$ remains proper reconstruction quality. Thus, we select our model variants in this range.

Quantization regularization λ_q The value of λ_q controls the strength of quantization regularization, which encour-

ages the model to use fewer bits to represent the abstract features. The ablation experiment on quantization regularization strength λ_q is presented in Table A10 and Fig. A12, the value of λ_q is set to $\{5 \times 10^{-4}, 1 \times 10^{-3}, 2 \times 10^{-3}, 3 \times 10^{-3}, 4 \times 10^{-3}\}$ in the experiments. Larger λ_q encourages the model to use fewer bits for feature representation \mathbf{f} and scaling controller \mathbf{s} , which reduces the model storage size stably and sacrifices reconstruction quality slowly in the range $[5 \times 10^{-4}, 2 \times 10^{-3}]$. Therefore, we choose $\lambda_q = 1 \times 10^{-3}$ for our default model Smol-GS-base.

B.2. Additional Quantitative Results

The overall quantitative comparison among all baselines on three benchmark data sets is presented as a scatter plot in Fig. A13. The results demonstrate that Smol-GS achieves competitive reconstruction quality with low memory footprints compared to other baselines.

Table A8. **Ablation study on feature dimension n_f .** Dimension 8 provides a good trade-off between size and quality.

Feature Dimension	MIP-NERF 360				TANKS AND TEMPLES				DEEP BLENDING			
	PSNR↑	SSIM↑	LPIPS↓	Size↓	PSNR↑	SSIM↑	LPIPS↓	Size↓	PSNR↑	SSIM↑	LPIPS↓	Size↓
$n_f = 4$	26.93	0.792	0.261	4.63	23.64	0.836	0.201	3.897	29.76	0.903	0.257	2.699
$n_f = 6$	27.03	0.800	0.251	6.284	23.83	0.841	0.194	5.295	29.74	0.905	0.255	3.788
$n_f = 8$	27.53	0.806	0.242	6.617	23.94	0.840	0.193	5.187	29.97	0.907	0.250	3.347
$n_f = 16$	27.47	0.806	0.243	9.171	24.14	0.849	0.184	8.722	29.91	0.907	0.249	4.432
$n_f = 32$	27.61	0.810	0.237	14.38	24.13	0.848	0.184	11.38	29.98	0.907	0.247	6.864

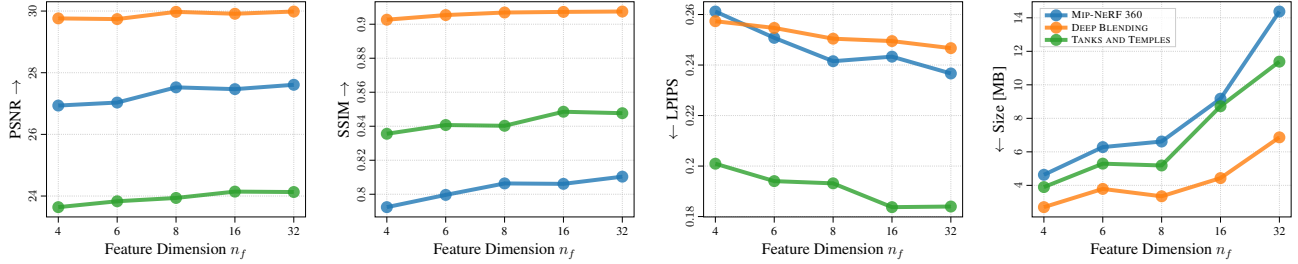


Figure A10. **Ablation study on feature dimension n_f .** In each subfigure, the x -axis represents different feature dimensions n_f , and the y -axis represents the corresponding metric values: PSNR, SSIM, LPIPS, Size (in MBs).

Table A9. **Ablation study on opacity regularization strength λ_o .**

Opacity Regularization	MIP-NERF 360				TANKS AND TEMPLES				DEEP BLENDING			
	PSNR↑	SSIM↑	LPIPS↓	Size↓	PSNR↑	SSIM↑	LPIPS↓	Size↓	PSNR↑	SSIM↑	LPIPS↓	Size↓
$\lambda = 1 \times 10^{-7}$	27.56	0.808	0.232	9.494	23.97	0.844	0.184	6.82	29.96	0.907	0.244	4.997
$\lambda = 2 \times 10^{-7}$	27.53	0.806	0.242	6.486	23.83	0.836	0.196	5.267	29.99	0.907	0.251	3.406
$\lambda = 3 \times 10^{-7}$	27.36	0.798	0.259	4.694	23.85	0.837	0.202	4.622	29.60	0.900	0.272	2.701
$\lambda = 4 \times 10^{-7}$	27.13	0.786	0.278	3.743	23.84	0.839	0.200	3.98	29.59	0.900	0.274	2.284
$\lambda = 5 \times 10^{-7}$	26.83	0.773	0.295	3.049	23.20	0.813	0.237	3.495	29.56	0.901	0.273	1.974

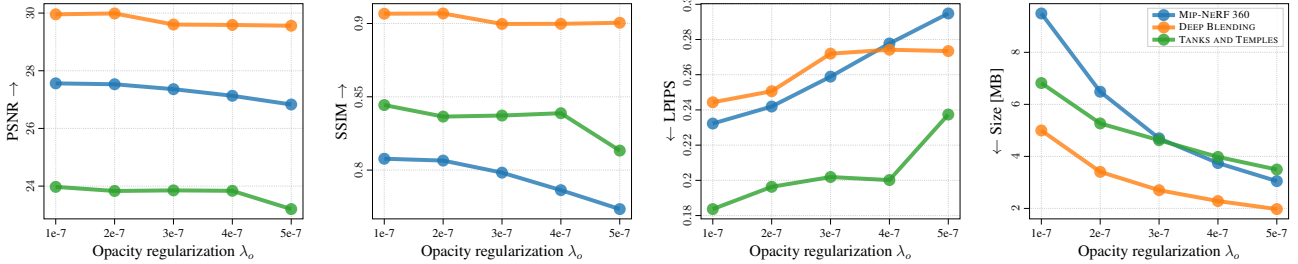


Figure A11. **Ablation study on opacity regularization strength λ_o .** In each subfigure, the x -axis represents different opacity regularization strength λ_o , and the y -axis represents the corresponding metric values: PSNR, SSIM, LPIPS, size (in MBs).

Table A10. **Ablation study on quantization regularization strength λ_q .**

Quantization Regularization	MIP-NERF 360				TANKS AND TEMPLES				DEEP BLENDING			
	PSNR↑	SSIM↑	LPIPS↓	Size↓	PSNR↑	SSIM↑	LPIPS↓	Size↓	PSNR↑	SSIM↑	LPIPS↓	Size↓
$\lambda_q = 5 \times 10^{-4}$	27.57	0.807	0.240	7.19	23.88	0.837	0.199	5.824	29.95	0.906	0.252	3.654
$\lambda_q = 1 \times 10^{-3}$	27.47	0.805	0.243	6.513	23.86	0.838	0.196	5.314	29.72	0.904	0.257	3.388
$\lambda_q = 2 \times 10^{-3}$	27.40	0.804	0.244	6.123	23.93	0.842	0.192	4.751	29.85	0.905	0.254	3.128
$\lambda_q = 3 \times 10^{-3}$	27.28	0.802	0.247	5.601	24.02	0.842	0.192	4.655	29.76	0.903	0.257	2.976
$\lambda_q = 4 \times 10^{-3}$	27.19	0.801	0.250	5.376	23.88	0.836	0.199	4.324	29.77	0.904	0.256	3.085

B.3. Additional Qualitative Results

The additional qualitative comparison among ground truth, 3DGS-30K, Smol-GS-base, and Smol-GS-small is presented

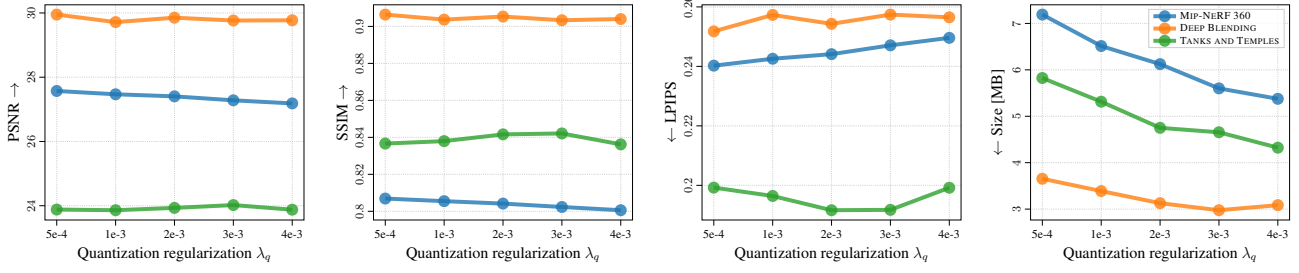


Figure A12. **Ablation study on quantization regularization strength λ_q .** In each subfigure, the x -axis represents different quantization regularization strength λ_q , and the y -axis represents the corresponding metric values: PSNR, SSIM, LPIPS, size (in MBs).

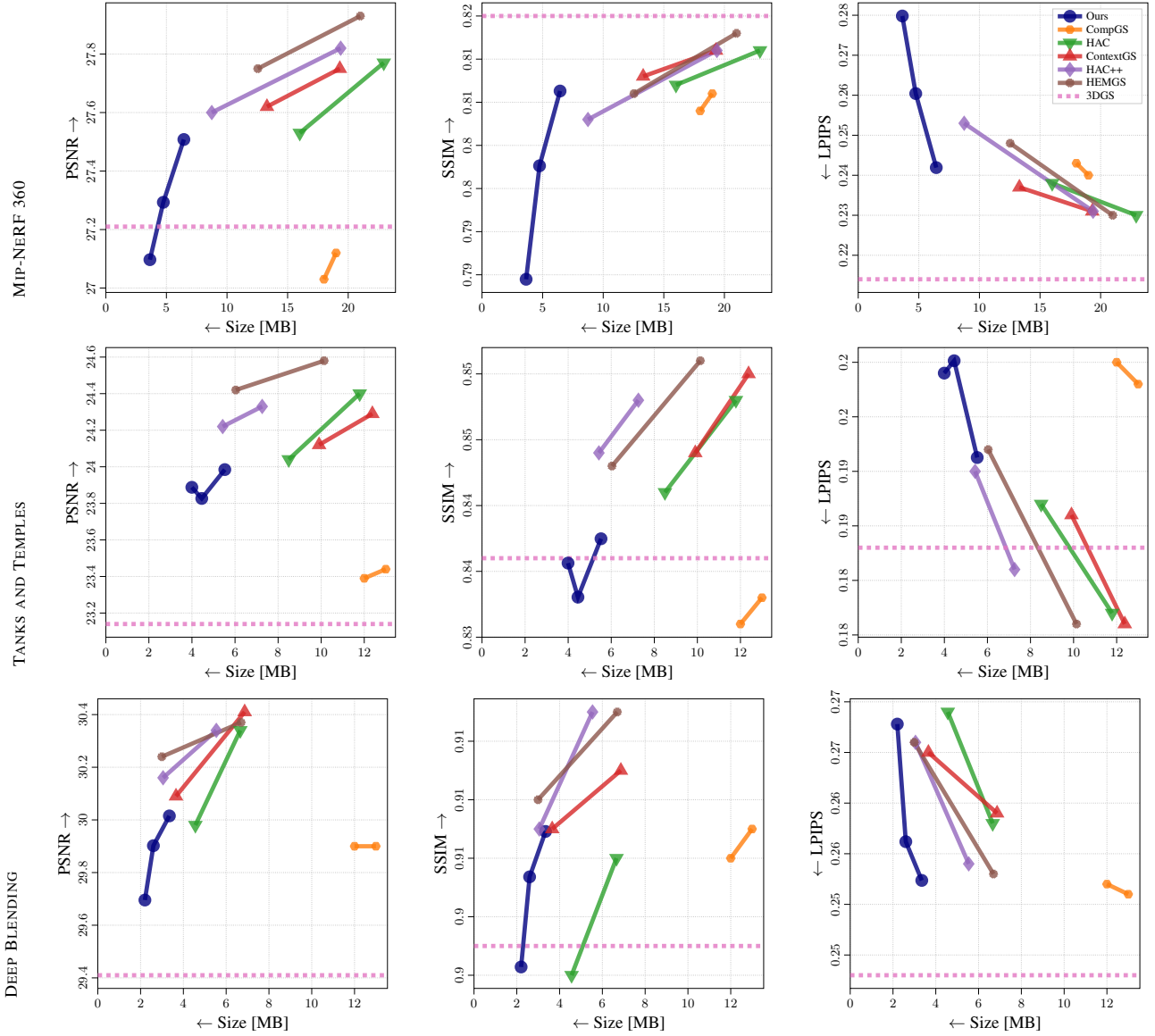


Figure A13. **Comparison of reconstruction quality across baselines.** In each subfigure, the x -axis represents the model size (in MBs), and the y -axis represents the corresponding metric values: PSNR (higher is better), SSIM (higher is better), LPIPS (lower is better). Different rows correspond to different benchmark data sets: MIP-NERF 360, TANKS AND TEMPLES, and DEEP BLENDING. Each line connects the results of a specific model over different hyperparameters (variants).

in Fig. A14. The results provide more details that Smol-GS preserves scene details with fewer artefacts than 3DGS-30K, even with smaller model sizes. Smol-GS-small loses some fine details compared to Smol-GS-base, but still maintains competitive visual quality.

B.4. Occupancy-Octree Analysis

The occupancy-octree learned in Sec. 3.2 generates a set of byte-codes during the encoding process. The statistical characteristics of the bytestream are analyzed in Fig. A15. The results show that most divisions generate fewer non-empty sub-boxes, indicating that the byte-codes are highly sparse and thus compressible by entropy encoding.

B.5. Encoding and Decoding Details

The per-scene encoding time, decoding time, and reconstruction quality for both Smol-GS-base and Smol-GS-small are summarized in Tables A11 to A16.

Table A11. Encoding time of each component of Smol-GS-base (in seconds) for each scene.

Encoding time (s)		Total	x	f	s	MLPs
MIP-NERF 360	Garden	3.984	0.273	2.391	1.211	0.018
	Bicycle	2.783	0.203	1.594	0.905	0.019
	Stump	2.747	0.189	1.428	1.001	0.020
	Bonsai	1.391	0.123	0.780	0.425	0.016
	Counter	1.754	0.126	0.998	0.537	0.015
	Kitchen	1.926	0.135	1.073	0.588	0.014
	Room	1.049	0.109	0.553	0.331	0.016
	Treehill	2.172	0.158	1.267	0.681	0.017
	Flowers	3.446	0.298	1.847	1.019	0.042
	Drjohnson	1.697	0.142	0.884	0.613	0.017
DEEP BLENDING	Playroom	0.826	0.082	0.418	0.272	0.016
	Train	2.200	0.105	1.268	0.762	0.014
TANKS AND TEMPLES	Truck	1.880	0.130	1.093	0.597	0.016

Table A12. Encoding time of each component of Smol-GS-small (in seconds) for each scene.

Encoding time (s)		Total	x	f	s	MLPs
MIP-NERF 360	Garden	2.980	0.200	1.794	0.906	0.017
	Bicycle	1.988	0.150	1.143	0.633	0.017
	Stump	1.800	0.145	1.020	0.576	0.019
	Bonsai	1.238	0.106	0.696	0.367	0.038
	Counter	1.545	0.147	0.873	0.472	0.014
	Kitchen	1.688	0.116	0.961	0.559	0.014
	Room	0.897	0.095	0.469	0.292	0.017
	Treehill	1.232	0.105	0.693	0.390	0.014
	Flowers	2.009	0.144	1.158	0.647	0.016
	Drjohnson	1.255	0.118	0.689	0.399	0.017
DEEP BLENDING	Playroom	0.666	0.075	0.322	0.233	0.015
	Train	1.766	0.100	1.032	0.579	0.013
TANKS AND TEMPLES	Truck	1.519	0.115	0.865	0.486	0.016

B.6. Interpretation of Features

The abstract features learned by Smol-GS-base are visualized in Fig. A16. The features are visualized by the dimension reduction technique and transformation. We can observe that the learned features capture meaningful optical captures and semantics.

Table A13. Decoding time of each component of Smol-GS-base (in seconds) for each scene.

Decoding time (s)		Total	x	f	s	MLPs
MIP-NERF 360	Garden	6.098	0.280	3.311	2.473	0.019
	Bicycle	4.290	0.185	2.317	1.759	0.018
	Stump	3.768	0.151	2.032	1.557	0.019
	Bonsai	2.209	0.099	1.258	0.829	0.016
	Counter	2.711	0.112	1.525	1.050	0.015
	Kitchen	2.850	0.114	1.568	1.141	0.016
	Room	1.584	0.084	0.803	0.675	0.017
	Treehill	3.391	0.140	1.871	1.354	0.018
	Flowers	5.181	0.209	2.921	2.017	0.019
	Drjohnson	2.393	0.118	1.154	1.096	0.018
DEEP BLENDING	Playroom	1.254	0.062	0.595	0.577	0.016
	Train	3.428	0.084	1.858	1.458	0.016
TANKS AND TEMPLES	Truck	2.866	0.111	1.559	1.171	0.017

Table A14. Decoding time of each component of Smol-GS-small (in seconds) for each scene.

Decoding time (s)		Total	x	f	s	MLPs
MIP-NERF 360	Garden	4.590	0.198	2.517	1.843	0.017
	Bicycle	3.041	0.126	1.663	1.227	0.017
	Stump	2.738	0.113	1.493	1.109	0.018
	Bonsai	1.871	0.085	1.040	0.722	0.017
	Counter	2.334	0.117	1.283	0.914	0.015
	Kitchen	2.705	0.101	1.512	1.069	0.015
	Room	1.383	0.074	0.691	0.598	0.016
	Treehill	2.022	0.079	1.107	0.815	0.015
	Flowers	3.246	0.120	1.840	1.261	0.017
	Drjohnson	1.816	0.097	0.905	0.792	0.016
DEEP BLENDING	Playroom	1.020	0.048	0.458	0.493	0.016
	Train	2.702	0.074	1.455	1.149	0.015
TANKS AND TEMPLES	Truck	2.445	0.090	1.358	0.975	0.016

Table A15. reconstruction quality per scene for Smol-GS-base

Reconstruction		PSNR↑	SSIM↑	LPIPS↓	Size↓
MIP-NERF 360	Garden	27.222	0.841	0.157	11.295
	Bicycle	24.869	0.730	0.291	7.985
	Stump	26.562	0.760	0.277	6.992
	Bonsai	32.378	0.942	0.190	3.723
	Counter	29.650	0.914	0.187	4.895
	Kitchen	31.232	0.925	0.130	5.234
	Room	31.439	0.921	0.207	2.789
	Treehill	22.969	0.637	0.367	6.063
	Flowers	21.250	0.586	0.371	8.986
	Drjohnson	29.645	0.908	0.248	4.553
DEEP BLENDING	Playroom	30.386	0.906	0.256	2.138
	Train	22.307	0.806	0.231	5.887
TANKS AND TEMPLES	Truck	25.662	0.879	0.151	5.164

Table A16. reconstruction quality per scene for Smol-GS-small

Reconstruction		PSNR↑	SSIM↑	LPIPS↓	Size↓
MIP-NERF 360	Garden	26.905	0.826	0.185	8.524
	Bicycle	24.594	0.707	0.325	5.544
	Stump	26.480	0.752	0.298	5.093
	Bonsai	32.229	0.941	0.193	3.245
	Counter	29.562	0.913	0.191	4.334
	Kitchen	30.603	0.920	0.139	4.737
	Room	31.441	0.920	0.213	2.363
	Treehill	22.730	0.628	0.404	3.279
	Flowers	21.094	0.573	0.396	5.595
	Drjohnson	29.592	0.907	0.249	3.496
DEEP BLENDING	Playroom	30.212	0.904	0.263	1.701
	Train	22.145	0.800	0.242	4.820
TANKS AND TEMPLES	Truck	25.509	0.876	0.159	4.090

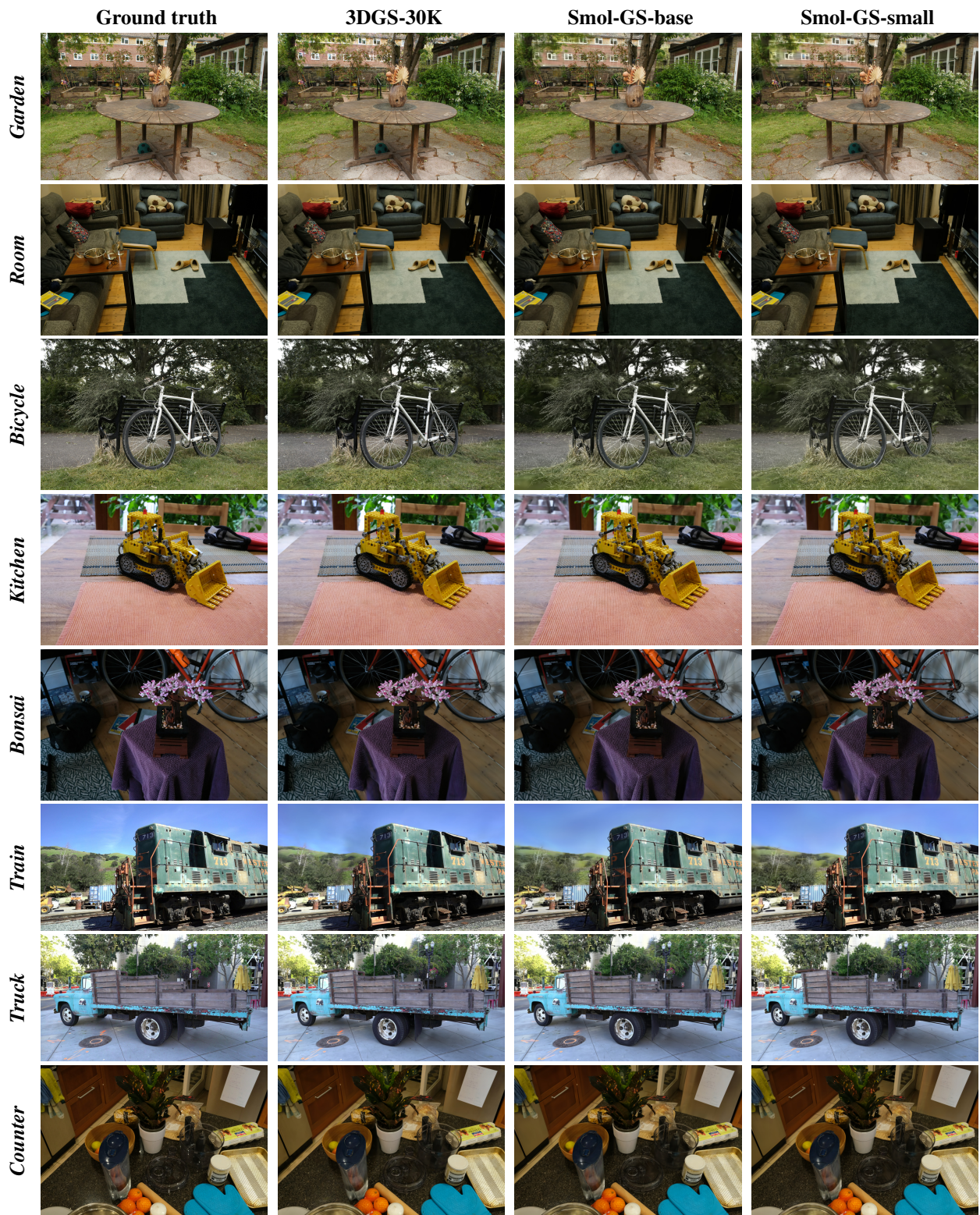


Figure A14. **Comparison of qualitative results** among the ground truth, 3DGS-30K, Smol-GS-base, and Smol-GS-small.

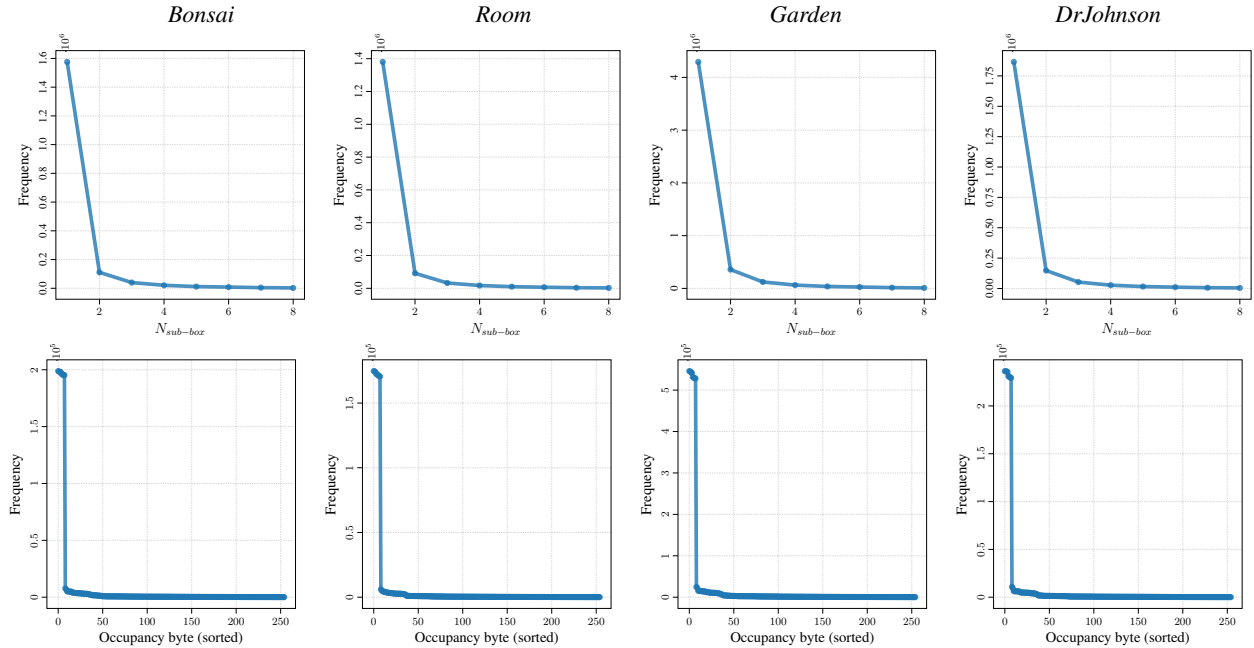


Figure A15. Statistical analysis of the occupancy-octree bytecodes on four example scenes: *Bonsai*, *Room*, *Garden*, *DrJohnson*. The occupancy-octree generates a series of bytecodes during the encoding process. Each bytecode denotes the existence of the subboxes of the corresponding division. The first row shows the histogram of the number of non-empty sub-boxes per division, and the second row shows the histogram of different bytecode values (sorted by frequency). Each column corresponds to a specific scene. The histograms indicate the strong sparsity of the occupancy-octree bytecodes shared by different scenes.

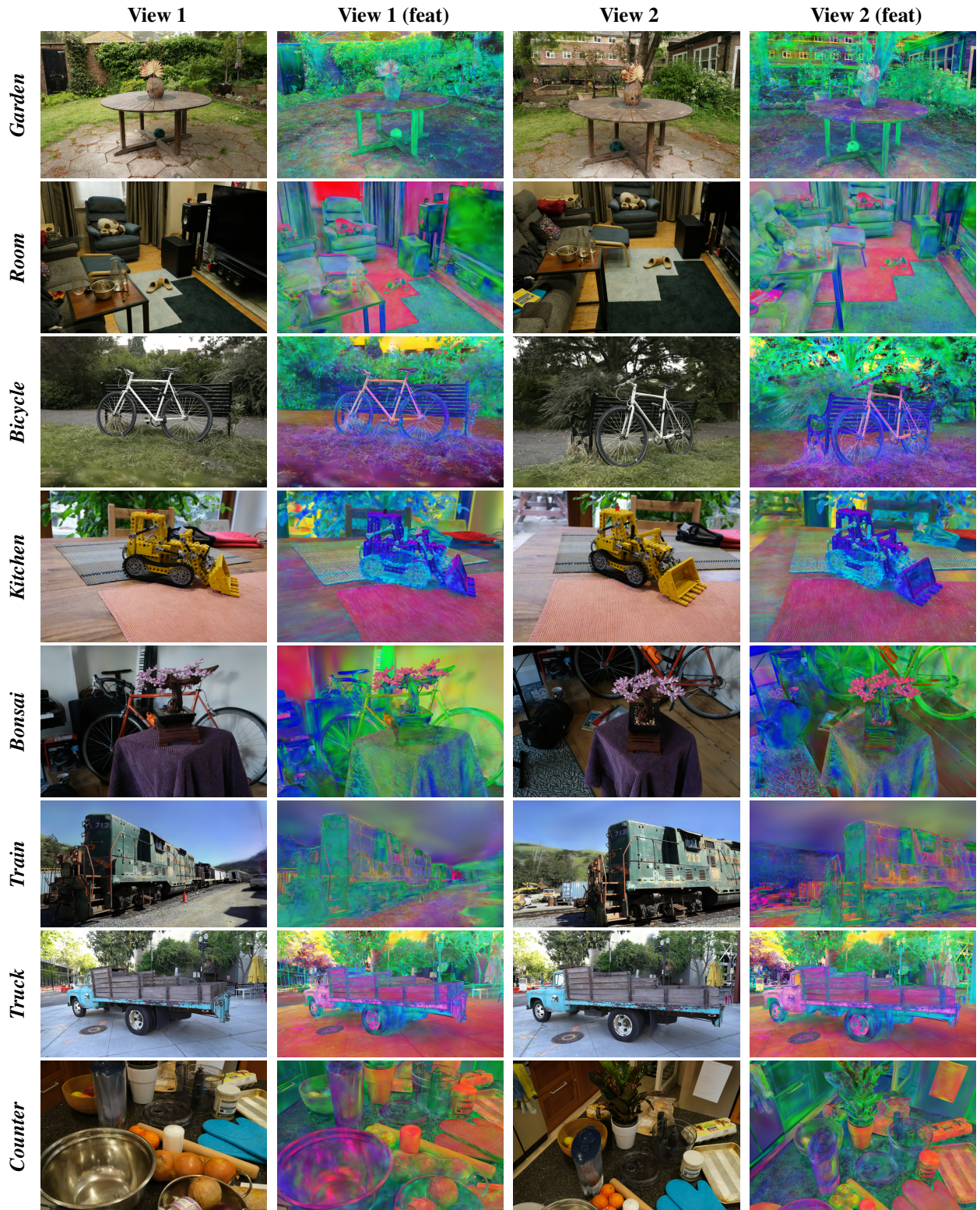


Figure A16. **Visualization of learned abstract features.** For each scene, we show two different views and their corresponding rendering image and feature visualizations. The features are visualized by mapping the 8-dimensional features to RGB colors using $\text{RGB} = \text{sigmoid}(\text{PCA}(\mathbf{f}))$.